

# Giant magnon spin conductivity approaching the two-dimensional transport regime in ultrathin yttrium iron garnet films

Xiangyang Wei (✉ [x.wei@rug.nl](mailto:x.wei@rug.nl))

University of Groningen <https://orcid.org/0000-0002-1651-4714>

**Obed Alves Santos**

University of Groningen

**Cristhian Humberto Sumba Lusero**

University of Groningen

**Gerrit Bauer**

University of Groningen

**Jamal Ben Youssef**

LabSTICC-UMR 6285

**Bart van Wees**

University of Groningen

---

**Letter**

**Keywords:**

**Posted Date:** January 6th, 2022

**DOI:** <https://doi.org/10.21203/rs.3.rs-1217468/v1>

**License:** © ⓘ This work is licensed under a Creative Commons Attribution 4.0 International License.

[Read Full License](#)

---

**Version of Record:** A version of this preprint was published at Nature Materials on September 22nd, 2022.  
See the published version at <https://doi.org/10.1038/s41563-022-01369-0>.

# Giant magnon spin conductivity approaching the two-dimensional transport regime in ultrathin yttrium iron garnet films

X-Y. Wei<sup>1,\*</sup>, O. Alves Santos<sup>1</sup>, C.H. Sumba Lusero<sup>1,†</sup>, G. E. W. Bauer<sup>1,2</sup>, J. Ben Youssef<sup>3</sup>, and B. J. van Wees<sup>1</sup>

<sup>1</sup>Physics of Nanodevices, Zernike Institute for Advanced Materials, University of Groningen, Nijenborgh 4, 9747 AG Groningen, The Netherlands

<sup>2</sup>WPI-AIMR & Institute for Materials Research & CSRN, Tohoku University, Sendai 980-8577, Japan

<sup>3</sup>Lab-STICC, CNRS- UMR 6285, Université de Bretagne Occidentale, 6 Avenue Le Gorgeu, 29238 Brest Cedex 3, France

\*e-mail: x.wei@rug.nl

†Current address: Leibniz Institute for Solid State and Materials Research, IFW, 01069 Dresden, Germany

1        **Conductivities are key material parameters that govern various types of transport (elec-**  
2 **tronic charge, spin, heat etc.) driven by thermodynamic forces. Magnons, the elementary ex-**  
3 **citations of the magnetic order, flow under the gradient of a magnon chemical potential<sup>1-3</sup> in**  
4 **proportion to a magnon (spin) conductivity  $\sigma_m$ . The magnetic insulator yttrium iron garnet**  
5 **(YIG) is the material of choice for efficient magnon spin transport. Here we report an unex-**  
6 **pected giant  $\sigma_m$  in record-thin YIG films with thicknesses down to 3.7 nm when the number**  
7 **of occupied two-dimensional (2D) subbands is reduced from a large number to a few, which**

8 corresponds to a transition from 3D to 2D magnon transport. We extract a 2D spin con-  
9 ductivity ( $\approx 1$  S) at room temperature, comparable to the (electronic) spin conductivity of  
10 the high-mobility two-dimensional electron gas in GaAs quantum wells at millikelvin tem-  
11 peratures<sup>4</sup>. Such high conductivities offer unique opportunities to develop low-dissipation  
12 magnon-based spintronic devices.

13 The spin current density in metals is the difference of the up- and down-spin charge current  
14 densities measured in  $A/m^2$ , which is driven by a gradient of the spin chemical potential (often  
15 called spin accumulation)  $\nabla\mu_s$ . The spin conductivity  $\sigma$ , defined as  $j_s = j_\uparrow - j_\downarrow = \sigma_s \nabla\mu_s/e$ , can  
16 be expressed in electrical units as S/m. In a magnetic insulator where charge currents are absent,  
17 each magnon carries angular momentum  $\hbar$ , which is equivalent to the spin current in metals carried  
18 by a pair of spin-up ( $+\hbar/2$ ) and spin-down ( $-\hbar/2$ ) electrons that flow in opposite directions. A  
19 magnon current  $j_m$  can be defined as its number current times electron charge  $e$ . In magnetic  
20 insulator-based spintronic devices, magnon spin currents are injected, detected, and modulated by  
21 microwave striplines or electric contacts made from a heavy metal for charge-spin conversion<sup>5-9</sup>.  
22 The corresponding spin conductivity, magnon conductivity  $\sigma_m$ , is the current density divided by  
23 the gradient of the magnon chemical potential. The unit of the magnon conductivity in  $j_m =$   
24  $\sigma_m \nabla\mu_m/e$ , where  $\mu_m$  is the magnon chemical potential, is then the same as that of electrons in  
25 a metal<sup>1</sup>. The value of  $\sigma_m = 4 \times 10^5$  S/m in a 210 nm thick YIG film at room temperature<sup>6</sup>  
26 corresponds to the electronic conductivity of bad metals.

27 The high magnetic and acoustic quality of magnetic insulators make them the ideal material

28 for all-magnon logical circuits and magnon-based quantum information<sup>10,11</sup>. An example of recent  
29 progress in magnon-based computing is an integrated magnonic half-adder based on 350 nm wide  
30 wave guides made from 85-nm-thick YIG films<sup>12</sup>. However, these devices operate with coherent  
31 magnons ( $\sim$  GHz) excited by narrow microwave striplines which can not be integrated into an all-  
32 electrical circuit. Therefore, it is attractive to inject magnons electrically<sup>13</sup>, but those are mainly  
33 thermal ( $\sim$  THz) and scatter much stronger at phonons. Also, scalability to smaller structure sizes,  
34 essential for future high-performance processing units, requires micro and nanofabrication in all  
35 dimensions. The first step is the growth of films of a few or even a single unit cell. Previously,  
36 magnon transport was reported in transistor structures on films down to about 10 nm, which shows  
37 that ultrathin films can maintain high quality and display intriguing non-linear magnon effects<sup>14,15</sup>.  
38 However, the scattering by surface roughness is expected to increase in even thinner films<sup>16</sup>.  
39 This could be an obstacle for magnon spin transport in ultrathin YIG films that hinders observation  
40 of a transition from three dimensional magnons to two dimensional magnon gas when the thermal  
41 wavelength  $\lambda_{\text{thermal}} = \sqrt{4\pi J_s / (k_B T)}$  ( $\sim 2$  nm at room temperature<sup>17</sup>) approaches the thickness of  
42 the films  $t_{\text{YIG}}$ , where  $J_s$  is spin-wave stiffness and  $k_B$  is Boltzmann constant.

43 Here we report measurements of the magnon conductivity of YIG films with thicknesses  
44 down to 3.7 nm. Much to our surprise, the magnon transport turns out to be strongly enhanced  
45 in the ultrathin regime. We report a drastical increase in magnon conductivity of up to  $\sigma_m =$   
46  $1.6 \times 10^8$  S/m at room temperature that even exceeds the electronic spin conductivity of high-  
47 purity copper. This increase is intimately connected to the small number of occupied subbands and  
48 apparent domination by the lowest subband in our films. These results can importantly boost the

49 performance of magnon-based information technology<sup>10,18</sup>.

50 We employ a non-local configuration<sup>6</sup> (Figure 1a) of two Pt thin film strips with length  $L$   
51 at a distance  $d$  on top of YIG films grown on gallium gadolinium garnet (GGG) by liquid phase  
52 epitaxy. An electric charge current  $I$  through the injector generates a transverse spin current due  
53 to the spin Hall effect<sup>19</sup>, resulting in a spin accumulation  $\mu_s$  in Pt at the interface to YIG. The  
54 injector-conversion coefficient  $\eta_{\text{inj}} = \mu_s/(eI)$  depends on the properties and dimensions of the Pt  
55 strip as explained in the Section I of the supplementary information (SI Section I). The effective  
56 interface spin conductance results from the exchange interaction across the interface and produces  
57 a magnon chemical potential  $\mu_m$  on the YIG side of the interface that acts as a *magnon source*,  
58 where  $\mu_m \approx \mu_s$  since the interface spin resistance can be ignored (see SI Section III). The detector  
59 electrode is a *magnon drain* that absorbs magnons and converts them into a spin current  $j_s$  entering  
60 the Pt detector electrode. The inverse spin Hall effect generates a detector voltage  $V_{\text{nl}}$  with detector-  
61 conversion coefficient  $\eta_{\text{det}} = V_{\text{nl}}/j_s^{\text{det}}$ . By reciprocity,  $\eta_{\text{inj}} = \eta_{\text{det}}$  when injector and detector  
62 contacts have the same properties (see SI Section I for details). Since the signal scales with  $L$ ,  
63 a normalized non-local resistance can be defined as  $R_{\text{nl}} = V_{\text{nl}}/(IL)$ . The magnon conductance  
64 follows from the measured non-local resistance

$$G_m = \frac{1}{\eta_{\text{inj}}\eta_{\text{det}}} \frac{V_{\text{nl}}}{I} = \frac{R_{\text{nl}}L}{\eta_{\text{inj}}\eta_{\text{det}}}. \quad (1)$$

65 The magnon conductivity  $\sigma_m$  as a function of the thickness  $t_{\text{YIG}}$  of the YIG films in Figure 1 then  
66 follows from the magnon spin conductance

$$\sigma_m = \frac{G_m d}{t_{\text{YIG}} L}. \quad (2)$$

67 For the films with  $t_{\text{YIG}}$  much smaller than the magnon relaxation length  $\lambda_m$  as well as the lateral  
 68 device dimension,  $\mu_m$  can be considered constant in the  $z$  direction . Therefore, we use following  
 69 equation to describe magnon diffusion<sup>6,20</sup>

$$R_{\text{nl}} = \frac{\sigma_m t_{\text{YIG}} \eta_{\text{inj}} \eta_{\text{det}}}{\lambda_m} \text{csch} \frac{d}{\lambda_m} \rightarrow \begin{cases} \frac{\sigma_m t_{\text{YIG}} \eta_{\text{inj}} \eta_{\text{det}}}{d} & \text{for } d \ll \lambda_m \\ \frac{2\sigma_m t_{\text{YIG}} \eta_{\text{inj}} \eta_{\text{det}}}{\lambda_m} \exp\left(-\frac{d}{\lambda_m}\right) & \text{for } d \gg \lambda_m \end{cases} . \quad (3)$$

70 When the spacing  $d$  is smaller than  $\lambda_m$ , it is the Ohmic regime in which the magnons are con-  
 71 served,  $R_{\text{nl}}(G_m) \sim d^{-1}$ . Otherwise, the signal decays exponentially as a function of distance due  
 72 to magnon relaxation.

73 We measure  $R_{\text{nl}}$  at room temperature as a function of an external in-plane magnetic field  
 74  $\mathbf{H}_{\text{ex}}$  with  $|\mathbf{H}_{\text{ex}}| = 50$  mT, which we rotate in the plane (Figure 1a). We modulate the AC current  
 75  $I$  by a low frequency (18 Hz) and detect the first/second harmonic signal  $V_{\text{nl}}(\omega)/V_{\text{nl}}(2\omega)$  by lock-  
 76 in amplifiers (see Methods).  $V_{\text{nl}}(2\omega)$  depends on the spin Seebeck generation and diffusion of  
 77 magnons under an inhomogeneous temperature profile, which renders interpretation difficult<sup>21,22</sup>  
 78 (see SI Section V). Therefore, we focus on  $V_{\text{nl}}(\omega)$  that follows the formula

$$R_{\text{nl}}^{1\omega}(\alpha) = R_{\text{nl}}^{1\omega} \cos^2 \alpha + R_0^{1\omega}, \quad (4)$$

79 where  $R_0^{1\omega}$  is an offset resistance (see Methods) and  $\alpha$  is the angle of  $\mathbf{H}_{\text{ex}}$  with the  $x$ -axis. In  
 80 Figure. 2, the the angle-dependent measurements in various thickness YIG films show that  $R_{\text{nl}}^{1\omega}$   
 81 becomes four times larger when the film is over fifty times thinner from 210 nm to 3.7 nm. We also  
 82 observe a strongly increased non-local signal in ultrathin films in Figure 3 as a function of contact  
 83 separation for a wide range of  $t_{\text{YIG}}$  including results on ultrathin YIG films for 400 nm wide Pt

84 strips and for thicker films  $t_{\text{YIG}} \geq 210 \text{ nm}$ <sup>6,23</sup>. Figure 4a emphasizes the dramatic enhancement of  
 85  $R_{\text{nl}}^{1\omega}$  for the thinnest films down to  $t_{\text{YIG}} = 3.7 \text{ nm}$  and fixed  $d = 2.5 \mu\text{m}$ , which can be attributed to  
 86 the  $t_{\text{YIG}}$  dependence of  $\sigma_m$  because  $\lambda_m > 2.5 \mu\text{m}$  for all thicknesses (see SI Section IV for details).  
 87  $R_{\text{nl}}^{1\omega}$  increases with decreasing thickness and saturates for both the thinnest and thickest films.

88 A finite-element model<sup>1</sup> can simulate the depth ( $z$ ) dependence of  $\mu_m$  when  $t_{\text{YIG}} > \lambda_m$  (see  
 89 SI Section I for details). This leads to a limiting  $\sigma_m \rightarrow 3 \times 10^4 \text{ S/m}$  in Figure 4b for thicker films,  
 90 which represents the bulk value. The simulated  $R_{\text{nl}}$  values for  $d = 2.5 \mu\text{m}$  in Figure 4c have been  
 91 fitted to  $R_{\text{nl}}^{1\omega}$  in Figure 4a by conductivities that are strongly enhanced in the regime  $t_{\text{YIG}} < \lambda_m$ .  
 92 For  $t_{\text{YIG}} = 3.7 \text{ nm}$ , the magnon conductivity  $\sigma_m = 1.6 \times 10^8 \text{ S/m}$  is *four orders of magnitude*  
 93 *larger* compared to the bulk value, exceeding the electronic conductivity of pure metals such as  
 94 copper with  $\sigma_e = 6 \times 10^7 \text{ S/m}$ <sup>24</sup>. The observed saturation at  $t_{\text{YIG}} \rightarrow 0$  appears to reflect an  
 95 increased role of surface roughness scattering that we do not model explicitly.

96 A magnon conductivity that diverges for  $t_{\text{YIG}} \rightarrow 0$  like  $\sigma_m \sim \sigma_m^{2\text{D}} t_{\text{YIG}}^{-1}$  simply suggests two-  
 97 dimensional transport. In Figure 4c, it shows that  $\sigma_m^{2\text{D}}$  saturates for  $t_{\text{YIG}} < 10 \text{ nm}$ , i.e. higher 2D  
 98 subbands do not contribute significantly even though they are still populated (see below). Extrapo-  
 99 lation to zero thickness leads to  $\sigma_m^{2\text{D}} \approx 1 \text{ S}$ . This value at room temperature is comparable to that of  
 100 the high-mobility two-dimensional electron gas at millikelvin temperatures, which is  $\sigma_e^{2\text{D}} \approx 1.4 \text{ S}$   
 101 in GaAs quantum wells<sup>4</sup>.

102 The magnons propagate in the plane with wave vector  $\mathbf{k}$  and form perpendicular standing spin  
 103 waves (PSSW) in  $z$  direction labeled by an integer  $n$ . The exchange interaction scales like  $\sim k^2$

104 and dominates the magnon dispersion  $\varepsilon_{nk}$  at thermal energies ( $\approx k_B T$ ) with small magnetodipolar  
 105 corrections. A magnon with energy  $\varepsilon_{nk} = \hbar\gamma D (k^2 + (n\pi/t_{\text{YIG}})^2)$  contributes to the conduction  
 106 proportional to its thermal occupation  $N_{nk} = 1/\{\exp[\varepsilon_{nk}/(k_B T)] - 1\}$ , where  $\hbar$  is the reduced  
 107 Planck constant and  $k_B$  is the Boltzmann constant. For YIG  $\gamma/2\pi = 28$  GHz/T and the spin wave  
 108 stiffness<sup>25</sup>  $D = 5 \times 10^{-17}$  Tm<sup>2</sup>. The highest occupied subband  $n$  defined as

$$n = \text{int} \left( \frac{t_{\text{YIG}}}{\pi} \sqrt{\frac{k_B T}{\hbar\gamma D}} \right) \quad (5)$$

109 at  $\varepsilon_{n0} < k_B T$  as a function of thickness<sup>26</sup>, where  $\text{int}(x)$  is the greatest integer no more than  $x$ . For  
 110  $t_{\text{YIG}} = 3.7$  nm, only three approximately 2D subbands are occupied at room temperature.

111 The simplest model for the magnon conductivity in  $\nu$  ( $=2, 3$ ) dimensions follows from the  
 112 Boltzmann equation with a constant relaxation time  $\tau$

$$\sigma_m^{(\nu)} = \frac{e^2 \tau^{(\nu)}}{k_B T} \int \frac{d\mathbf{k}}{(2\pi)^\nu} \left( \frac{\partial \varepsilon_k}{\hbar \partial k_z} \right)^2 \frac{e^{\varepsilon_k/(k_B T)}}{(e^{\varepsilon_k/(k_B T)} - 1)^2} \quad (6)$$

113 where  $\varepsilon_k = \hbar\gamma D k^2$ . Magnetic freeze-out experiments show that the contributions from the low-  
 114 frequency magnons ( $\sim$  GHz) is significant even at room temperature, presumably reflecting low  
 115 mobilities of thermal exchange magnons<sup>27-29</sup>. This can be represented by a high momentum cut-  
 116 off  $K_\infty \sim 1/\text{nm}$  at magnon frequencies  $\varepsilon_\infty/\hbar \sim$  THz. In the high temperature limit  $k_B T \gg \varepsilon_k$   
 117 the conductivities do not depend on  $\gamma D$ :

$$\sigma_m^{(3)} = \frac{2e^2 k_B T \tau^{(3)}}{3\hbar^2 \pi^2} K_\infty, \quad (7)$$

$$\sigma_m^{(2)} = \frac{e^2 k_B T \tau^{(2)}}{\pi \hbar^2} \log \frac{K_\infty}{K_0}, \quad (8)$$

118 where  $K_0$  is a low momentum cutoff by the magnon gap of  $\varepsilon_0/\hbar \sim$  GHz. By equating these  
 119 equations with the experimental results  $\sigma_m^{(3)} \approx 3 \times 10^4$  S/m and the present  $\sigma_m^{(2)} \approx 1$  S and using  
 120

121 the scattering times as adjustable parameters, we arrive at  $\tau^{(3)} \approx 40$  fs and  $\tau^{(2)} \approx 0.1$  ns. The short  
122 scattering time in three dimensions can be explained by highly efficient magnon-phonon scattering  
123 at room temperature<sup>1</sup>. While the high-momentum cut-off plays an important role in 3 dimensions,  
124 the near independence of  $\sigma_m^{(2)}$  emphasizes the importance of the near band-gap excitations for  
125 transport in two dimensions. Coherent magnons excited at GHz frequencies can propagate over  
126 cm's in spite of their small group velocity because they scatter only weakly at phonons<sup>30</sup>. Their  
127 contribution has a much larger effect on transport in ultrathin films than in the bulk, which is  
128 consistent with the magnetic field and temperature dependence reported in the SI. The estimated  
129 scattering time of  $\tau^{(2)} = 0.1$  ns may be limited by the film roughness scattering. The precise  
130 mechanism can be elucidated only by more extensive experimental and theoretical studies of the  
131 temperature and field dependence.

132 While magnon-based devices do not suffer from Joule heating, magnon transport is not  
133 dissipationless<sup>6,31</sup> even for transport on length scales shorter than the magnon relaxation length  
134 where magnons are conserved. The observed giant magnon conductivity is therefore excellent  
135 news, implying low dissipation from magnon-phonon scattering even at room temperature. Ultra-  
136 thin films can therefore be driven with relative ease into the non-linear regime in e.g. magnon spin  
137 transistors<sup>14,15</sup>, facilitating electrically-induced magnon Bose-Einstein condensation and magnon  
138 spin superfluidity<sup>32-34</sup>. The robustness of the transport of the magnetic order for thin films of close  
139 to the monolayer thickness should allow magnon transport in nanostructures such as constrictions,  
140 wires and dots with feature sizes of a few nanometer without loss of magnetic functionality.

## 141 **Methods**

142 **Fabrication** The YIG films are grown on  $\text{Gd}_3\text{Ga}_5\text{O}_{12}$  (GGG) substrates by liquid-phase epitaxy  
143 (LPE) at the Université de Bretagne Occidentale in Brest, France, with thicknesses from 3.7 nm  
144 to 53 nm. The effective magnetization  $M_{\text{eff}}$  ( $H_{\text{k}} - 4\pi M_{\text{s}}$ ) and the magnetic relaxation (intrinsic  
145 damping parameter  $\alpha$  and extrinsic inhomogeneous linewidth  $\Delta H_{\text{in}}$ ) are determined by broadband  
146 ferromagnetic resonance (FMR) in the frequency range 2-40 GHz (see SI Section IV). The device  
147 patterns are written by three e-beam lithography steps, each followed by a standard deposition  
148 and lift-off procedure. The first step produces a Ti/Au marker pattern, used to align the subse-  
149 quent steps. The second step defines the platinum injector and detector strips, as deposited by dc  
150 sputtering in an Ar+ plasma at an argon pressure with thickness  $\sim 8$  nm for all devices. The third  
151 step defines 5/75 nm Ti/Au leads and bonding pads, deposited by e-beam evaporation. Devices  
152 have an injector/detector length  $L = 30/25 \mu\text{m}$  and the strip widths  $W$  are 400 nm for series A  
153 and 100 nm for series B. The experimental results in main text are obtained from series A. The  
154 distance-dependent non-local resistances for series B can be found in SI Section III.

155 **Measurements** All measurements were carried out by means of three SR830 lock-in amplifiers  
156 using excitation frequency of 18 Hz. The lock-in amplifiers are set up to measure the first and sec-  
157 ond harmonic responses of the sample. Current was sent to the sample using a custom built current  
158 source, galvanically isolated from the rest of the measurement equipment. Voltage measurements  
159 were made using a custom-built pre-amplifier (gain  $10^3$ ) and amplified further using the lock-in  
160 systems. The typical excitation currents applied to the samples are  $200 \mu\text{A}$  (RMS) for series A and

161 20  $\mu\text{m}$  for series B. The in-plane coercive field of the YIG  $B_c$  is below 10 mT for all YIG samples,  
162 and we apply an external field to orient the magnetization using a physical property measurement  
163 system (PPMS). The samples are mounted on a rotatable sample holder with stepper motor. All  
164 experimental data in the main text have been collected at 300 K (room temperature) at an applied  
165 magnetic field of 50 mT.

166 **Simulations** Our finite-element model implements the magnon diffusion equation in insulators  
167 in order to simulate transport of electrically injected magnons. We carried out the simulations  
168 by COMSOL MULTIPHYSICS (version 5.4) software package with technical details in the SI  
169 Section I.

## 170 **Acknowledgements**

171 We acknowledge the helpful discussion with J. Shan and T. Yu. We acknowledge the technical  
172 support from J. G. Holstein, H. de Vries, H. Adema, T. Schouten and A. Joshua. This work is  
173 part of the research programme "Skyrmionics" with project number 170, which is financed by the  
174 Dutch Research Council (NWO). The support by NanoLab NL and the Spinoza Prize awarded in  
175 2016 to B. J. van Wees by NWO is also gratefully acknowledged. G.B. was supported by JSPS  
176 Kakenhi Grant 19H00645.

177 **Author contributions**

178 B.J.v.W. and X.W. conceived the experiments. X.W. designed and carried out the experiments,  
179 with help from O.A.S. J.B.Y. supplied the YIG samples used in the fabrication of devices. X.W.,  
180 O.A.S., C.H.S.L., G.E.W.B. and B.J.v.W. were involved in the analysis. X.W. wrote the paper with  
181 O.A.S., G.E.W.B. and B.J.v.W. All authors commented on the manuscript.

182 **References**

- 184 1. Cornelissen, L. J., Peters, K. J. H., Bauer, G. E. W., Duine, R. A. & van Wees, B. J. Magnon  
185 spin transport driven by the magnon chemical potential in a magnetic insulator. *Phys. Rev. B*  
186 **94**, 014412 (2016).
- 187 2. Chunhui, D. *et al.* Control and local measurement of the spin chemical potential in a magnetic  
188 insulator. *Science* **357**, 195–198 (2017).
- 189 3. Olsson, K. S. *et al.* Pure spin current and magnon chemical potential in a nonequilibrium  
190 magnetic insulator. *Phys. Rev. X* **10**, 021029 (2020).
- 191 4. Chung, Y. J. *et al.* Ultra-high-quality two-dimensional electron systems. *Nature Materials* **20**,  
192 632–637 (2021).
- 193 5. Brataas, A., van Wees, B., Klein, O., de Loubens, G. & Viret, M. Spin insulatronics. *Physics*  
194 *Reports* **885**, 1–27 (2020).

- 195 6. Cornelissen, L. J., Liu, J., Duine, R. A., Ben Youssef, J. & van Wees, B. J. Long-distance  
196 transport of magnon spin information in a magnetic insulator at room temperature. *Nature*  
197 *Physics* **11**, 1022–1026 (2015).
- 198 7. Lebrun, R. *et al.* Tunable long-distance spin transport in a crystalline antiferromagnetic iron  
199 oxide. *Nature* **561**, 222–225 (2018).
- 200 8. Chumak, A. V., Serga, A. A. & Hillebrands, B. Magnon transistor for all-magnon data pro-  
201 cessing. *Nature Communications* **5**, 4700 (2014).
- 202 9. Cornelissen, L. J., Liu, J., van Wees, B. J. & Duine, R. A. Spin-current-controlled modulation  
203 of the magnon spin conductance in a three-terminal magnon transistor. *Phys. Rev. Lett.* **120**,  
204 097702 (2018).
- 205 10. Barman, A. *et al.* The 2021 Magnonics Roadmap. *Journal of Physics: Condensed Matter* **33**,  
206 413001 (2021).
- 207 11. Chumak, A. *et al.* Roadmap on Spin-Wave Computing. Preprint at:  
208 <https://arxiv.org/abs/2111.00365> (2021).
- 209 12. Wang, Q. *et al.* A magnonic directional coupler for integrated magnonic half-adders. *Nature*  
210 *Electronics* **3**, 765–774 (2020).
- 211 13. Althammer, M. All-electrical magnon transport experiments in magnetically ordered insula-  
212 tors. *physica status solidi (RRL) –Rapid Research Letters* **15**, 2100130 (2021).

- 213 14. Wimmer, T. *et al.* Spin transport in a magnetic insulator with zero effective damping. *Phys.*  
214 *Rev. Lett.* **123**, 257201 (2019).
- 215 15. Liu, J., Wei, X.-Y., Bauer, G. E. W., Youssef, J. B. & van Wees, B. J. Electrically induced  
216 strong modulation of magnon transport in ultrathin magnetic insulator films. *Phys. Rev. B* **103**,  
217 214425 (2021).
- 218 16. Yu, T., Sharma, S., Blanter, Y. M. & Bauer, G. E. W. Surface dynamics of rough magnetic  
219 films. *Phys. Rev. B* **99**, 174402 (2019).
- 220 17. Cherepanov, V., Kolokolov, I. & L'vov, V. The saga of YIG: Spectra, thermodynamics, inter-  
221 action and relaxation of magnons in a complex magnet. *Physics Reports* **229**, 81–144 (1993).
- 222 18. Li, Y. *et al.* Hybrid magnonics: Physics, circuits, and applications for coherent information  
223 processing. *Journal of Applied Physics* **128**, 130902 (2020).
- 224 19. Sinova, J., Valenzuela, S. O., Wunderlich, J., Back, C. H. & Jungwirth, T. Spin Hall effects.  
225 *Rev. Mod. Phys.* **87**, 1213–1260 (2015).
- 226 20. Takahashi, S. & Maekawa, S. Spin injection and detection in magnetic nanostructures. *Phys.*  
227 *Rev. B* **67**, 052409 (2003).
- 228 21. Uchida, K. *et al.* Observation of the spin Seebeck effect. *Nature* **455**, 778–781 (2008).
- 229 22. Gomez-Perez, J. M., Vélez, S., Hueso, L. E. & Casanova, F. Differences in the magnon  
230 diffusion length for electrically and thermally driven magnon currents in  $Y_3Fe_5O_{12}$ . *Phys.*  
231 *Rev. B* **101**, 184420 (2020).

- 232 23. Shan, J. *et al.* Influence of yttrium iron garnet thickness and heater opacity on the nonlocal  
233 transport of electrically and thermally excited magnons. *Phys. Rev. B* **94**, 174437 (2016).
- 234 24. Laughton, M. A. & Say, M. G. *Electrical engineer's reference book* (Elsevier, 2013).
- 235 25. Klingler, S. *et al.* Measurements of the exchange stiffness of YIG films using broadband fer-  
236 romagnetic resonance techniques. *Journal of Physics D: Applied Physics* **48**, 015001 (2014).
- 237 26. Stamps, R. & Camley, R. *Solid State Physics*. No. Volume 65 in Solid State Physics (Elsevier  
238 Science, 2014).
- 239 27. Kikkawa, T. *et al.* Critical suppression of spin Seebeck effect by magnetic fields. *Phys. Rev.*  
240 *B* **92**, 064413 (2015).
- 241 28. Jin, H., Boona, S. R., Yang, Z., Myers, R. C. & Heremans, J. P. Effect of the magnon dispersion  
242 on the longitudinal spin Seebeck effect in yttrium iron garnets. *Phys. Rev. B* **92**, 054436 (2015).
- 243 29. Jamison, J. S. *et al.* Long lifetime of thermally excited magnons in bulk yttrium iron garnet.  
244 *Phys. Rev. B* **100**, 134402 (2019).
- 245 30. Streib, S., Vidal-Silva, N., Shen, K. & Bauer, G. E. W. Magnon-phonon interactions in mag-  
246 netic insulators. *Phys. Rev. B* **99**, 184442 (2019).
- 247 31. Man, H. *et al.* Direct observation of magnon-phonon coupling in yttrium iron garnet. *Phys.*  
248 *Rev. B* **96**, 100406 (2017).
- 249 32. Bender, S. A., Duine, R. A. & Tserkovnyak, Y. Electronic Pumping of Quasiequilibrium  
250 Bose-Einstein-Condensed Magnons. *Phys. Rev. Lett.* **108**, 246601 (2012).

- 251 33. Demokritov, S. O. *et al.* Bose–Einstein condensation of quasi-equilibrium magnons at room  
252 temperature under pumping. *Nature* **443**, 430–433 (2006).
- 253 34. Divinskiy, B. *et al.* Evidence for spin current driven Bose-Einstein condensation of magnons.  
254 *Nature Communications* **12**, 6541 (2021).

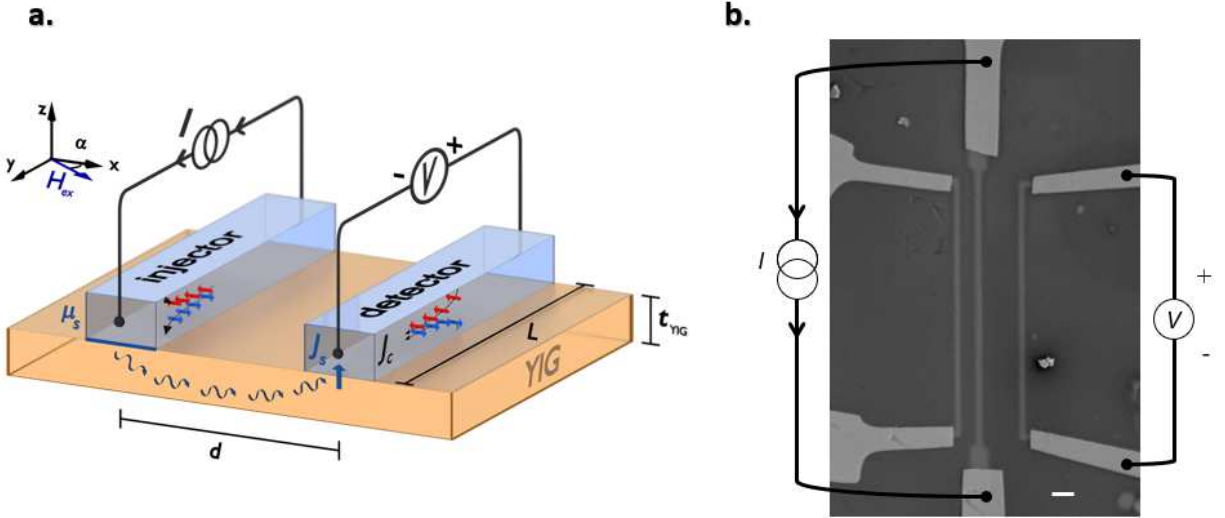


Figure 1: Device layout: **a)** Schematic representation of the experimental geometry. Two Pt strips deposited on top of YIG serve as magnon detector and injector via the direct and inverse spin hall effect. A low-frequency ac current with rms value of  $I_{ac}$  through the left Pt strip injects magnons. The center-to-center distance of the injector and the detector is  $d$  and the length of the injector/detector is  $L$ . A spin accumulation  $\mu_s$  is formed at Pt|YIG interface due to the SHE when a charge current passes through the injector and excites magnon non-equilibrium underneath the injector. The diffusive magnons are absorbed at the drain, which induce a spin current density  $j_s$ . Using a lock-in technique, the first harmonic voltage is measured simultaneously by the right Pt strip, i.e. a magnon detector.  $\alpha$  is the angle of external magnetic field  $H_{ex}$ . **b)** SEM image of the geometry. The parallel vertical lines are the platinum injector and detector, and they are contacted by gold leads. Current and voltage connections are indicated schematically. The scale bar represents  $2 \mu\text{m}$ .

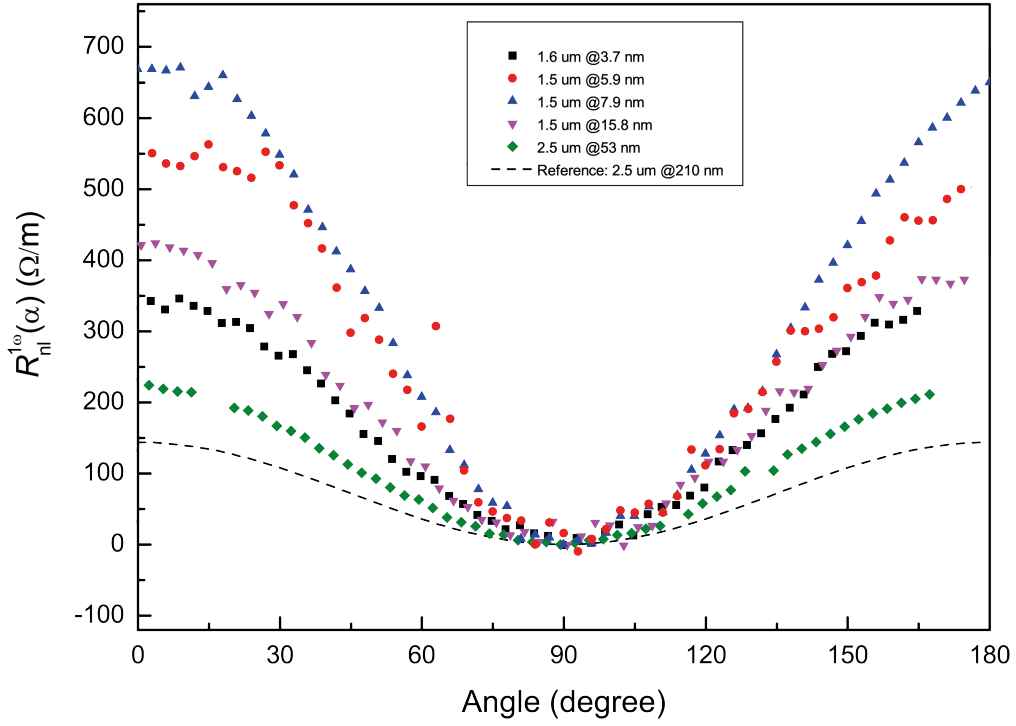


Figure 2: Dependence of non-local resistance on magnetization direction on ultrathin YIG films, for short center-to-center distances between the injector and the detector. The offset  $R_0^{1\omega}$  in Eq.4 has been subtracted. This shows  $R_{nl}^{1\omega}$  increases with decreasing thickness. Comparing with the reference from Cornelissen et al.<sup>6</sup>,  $R_{nl}^{1\omega}$  significantly increases in ultrathin films.

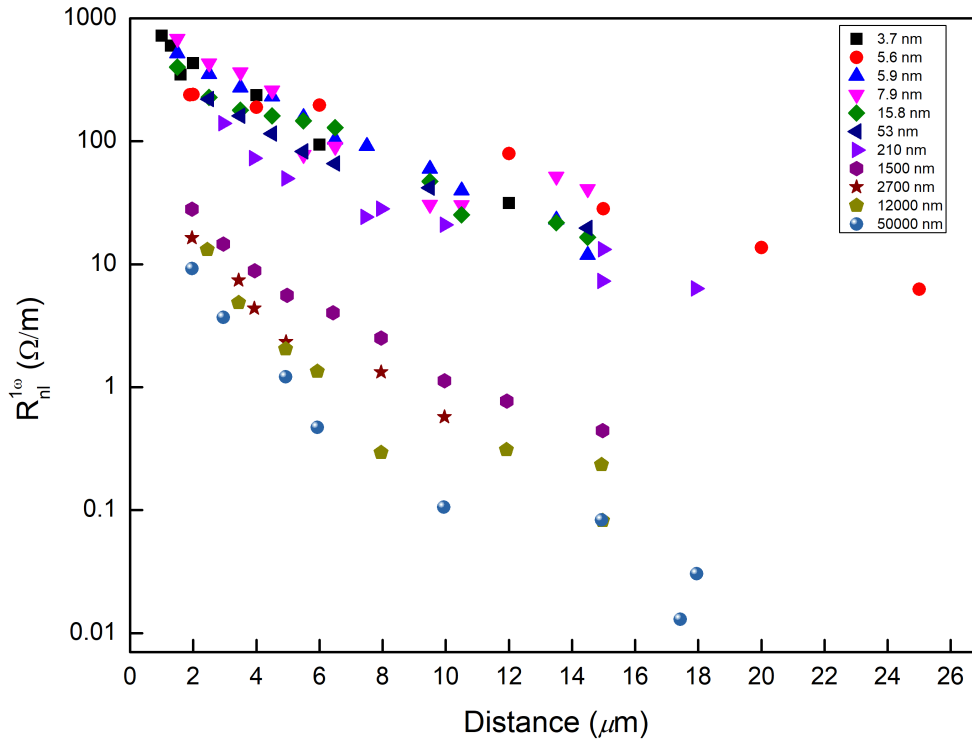


Figure 3: Non-local resistance as a function of injector-detector distance of the samples of series A and  $t_{\text{YIG}}$  varying from 3.7 nm to 50000 nm. The width of injector/detector is 400 nm. The results for  $t_{\text{YIG}} \geq 210$  nm are adopted from Cornelissen et al.<sup>6</sup> and Shan et al.<sup>23</sup>.

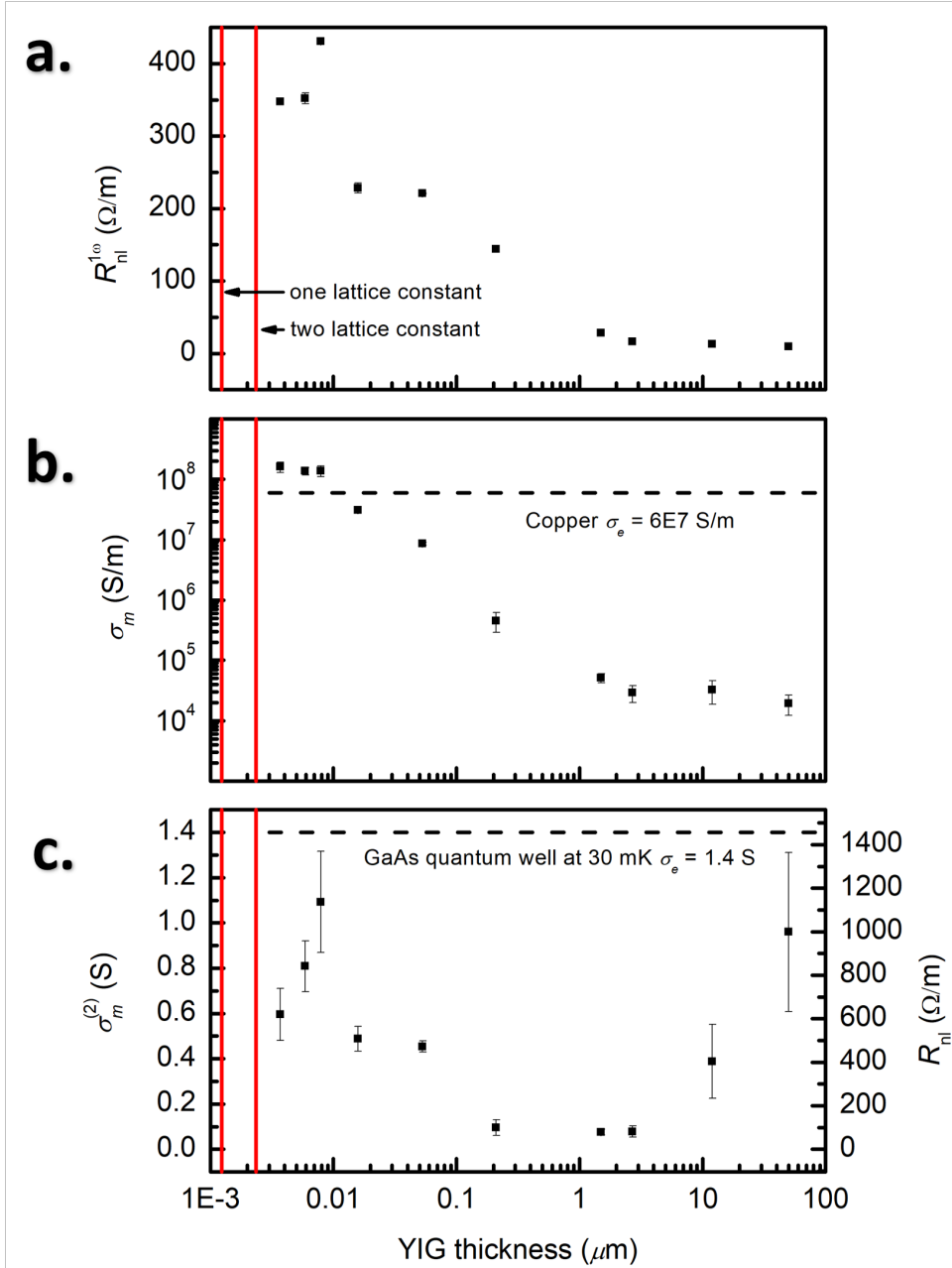


Figure 4: **a)** The non-local resistance  $R_{\text{nl}}^{1\omega}$  at  $d = 2.5 \mu\text{m}$  as a function of  $t_{\text{YIG}}$ . The results for  $t_{\text{YIG}} \geq 210 \text{ nm}$  are adopted from Cornelissen et al.<sup>6</sup> and Shan et al.<sup>23</sup>. **b)** Thickness dependence of the magnon conductivity  $\sigma_m$  obtained by the best fit for different distances with statistical error bars. **c)** Thickness dependence of the 2-dimension spin conductance  $\sigma_m^{(2)}$  and the non-local resistance  $R_{\text{nl}}$  from the simulation, values based on the best fit for the magnon conductivity. The saturation at  $t_{\text{YIG}} \rightarrow 0$  indicates that the film approaches the two-dimensional regime in ultrathin limit. The obtained error bar here means the range of the best fitting results for the non-local resistance we can get from the FEM simulations (see SI Section II).

## Supplementary Files

This is a list of supplementary files associated with this preprint. Click to download.

- [Supplementary.pdf](#)